Power Electronic Systems
Laboratory

IEEE Power and Energy Technology Systems Journal, Vol. 5, No. 4, pp. 139-147, December 2018

Analysis and Modeling of Eddy-Current Couplings for Auxiliary Power Generation on a Freight Train Wagon

M. Flankl,
A. Tüysüz,
C. Gong,
T. Stolz,
J. W. Kolar

Eidgenössische Technische Hochschule Zürich
Swiss Federal Institute of Technology Zurich

Received 18 June 2018; accepted 13 September 2018. Date of publication 20 September 2018; date of current version 11 December 2018.

Digital Object Identifier 10.1109/JPETS.2018.2871629

Analysis and Modeling of Eddy-Current Couplings for Auxiliary Power Generation on a Freight Train Wagon

MICHAEL FLANKL[1] (Student Member, IEEE), ARDA TÜYSÜZ[1] (Member, IEEE), CHENG GONG[2] (Student Member, IEEE), TIBOR STOLZ[1], AND JOHANN W. KOLAR[1] (Fellow, IEEE)

[1]Power Electronic Systems Laboratory, Swiss Federal Institute of Technology (ETH) Zurich, 8092 Zürich, Switzerland
[2]Georgia Institute of Technology, Atlanta, GA 30332 USA

CORRESPONDING AUTHOR: M. FLANKL (flankl@lem.ee.ethz.ch)

ABSTRACT The subject of this paper is a non-coaxial eddy-current coupling, which can be utilized on a freight train wagon for generating auxiliary power in the range of several Watts. The coupling comprises a wheel with radially magnetized permanent magnets, which is positioned in the vicinity of the wagon's wheel, and extracts kinetic energy when the train is in motion. A computational method for solving the 3-D problem of the eddy-current coupling is presented. Maxwell's equations for calculating the excited eddy currents are solved in the Fourier domain with a semi-analytical method (SAM), resulting in computationally efficient simulations. In a case study, the SAM shows 500 times faster simulation times, compared to a 3-D transient eddy-current finite-element method simulation, carried out with a commercially available software. The SAM is verified with measurements taken on two hardware prototypes. Furthermore, in order to generalize the study, a $\rho\eta$-Pareto optimization of the system is conducted for relaxed design space boundaries, an output power of $P = 10\,\mathrm{W}$, a C45E steel wheel with $v = 80\,\mathrm{km/h}$ surface velocity, and $g = 3\,\mathrm{mm}$ air gap. It is shown that a power density up to $0.8\,\mathrm{kW/dm^3}$ ($13\,\mathrm{W/in^3}$) and a transfer efficiency up to 60% can be achieved using the proposed system.

INDEX TERMS Eddy-current coupling, railway application, eddy currents, linear motors, energy harvesting.

I. INTRODUCTION

GENERATING electrical energy for auxiliary purposes directly at the location of consumption allows omitting battery supply systems and/or power supply cables as well as power conversion stages [1], [2]. Power in the microwatt or milliwatt range could be obtained by utilizing established energy-harvesting methods [3], [4], however, the achievable output power is too low for many applications and only allows one to supply ultra-low-power (sensing) applications. In the case of a freight train, watt-range auxiliary power could be utilized for e.g. powering actuators in an anti-lock braking system or a condition monitoring system of the car or loaded goods. In a traditional scenario, auxiliary power is supplied from the locomotive; however, in this case, power supply cables need to be installed on each wagon. Moreover, connecting electric supply plugs between each wagon can be expensive due to wear out of the plugs and the labor cost for the coupling procedure.

Auxiliary power generation systems, as illustrated in Fig. 1, overcome the aforementioned drawbacks. Such systems comprise

- a non-coaxial eddy-current coupling,
- a generator, and
- an active rectifier for conditioning the extracted electric power.

A non-coaxial eddy-current coupling is established between the wagon's wheel and radially magnetized permanent magnets (PM), which are mounted on a shaft that is free to rotate around its axis. When the wagon's wheel rotates, eddy currents are induced on its moving conductive surface (MCS). The reaction force acting on the magnets makes the PM wheel rotate. Fig. 2 illustrates such system.

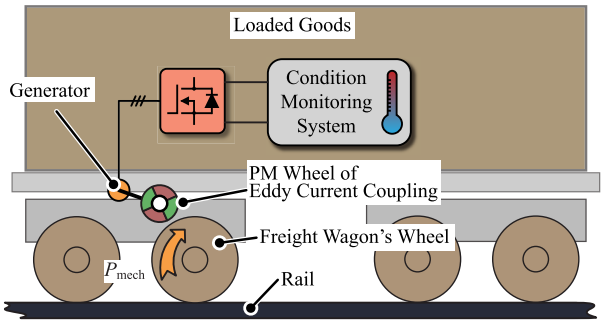

FIGURE 1. Application example of the eddy-current coupling on a freight train for coupling the wagon's wheel with an auxiliary power generator in a contactless fashion.

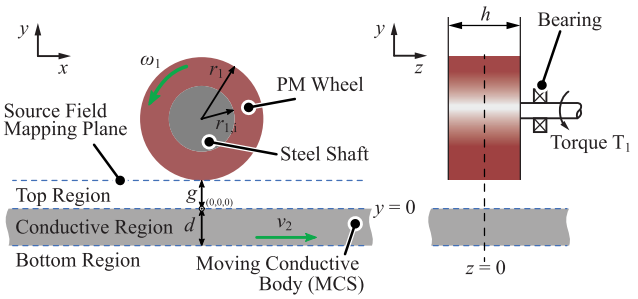

FIGURE 2. Illustration of the permanent magnet (PM) wheel, which becomes an eddy-current coupling together with the moving conductive surface (MCS). Conductive and non-conductive regions, used for deriving the model are labeled and the source field of the PM wheel is mapped on top of "top region" in the semi-analytical method (SAM) simulation.

Reference [5] proposes a similar concept for powering a low-power lighting unit, where the generator is implemented as a coil around the PM wheel. The merit of the system of Fig. 1 is that the wagon's wheel does not need any modification, nor is it in mechanical contact with the PM wheel as the power is extracted electromagnetically. Crucial for the operation is that eddy currents are excited in the MCS/wheel. Therefore, a non-zero time derivative of magnetic flux must penetrate the MCS (in its local, moving coordinate system).

The coupling's operation can be illustrated, considering the loading of the system, i.e. when the PM wheel delivers a torque to an electric generator. In this case, the PM wheel slows down and a higher surface speed difference between MCS and PM wheel appears. The derivative of magnetic flux increases and eddy currents settle at a higher magnitude. It will lead to an increased torque on the PM wheel, i.e. a new operating point with higher transferred torque is reached.

Co-axial eddy-current couplings are studied and optimized extensively in literature for various applications [6]–[8]. An initial characterization of a non-coaxial eddy-current coupling in combination with an aluminum MCS can be found e.g. in [9]. Moreover, Paudel analyzes a PM wheel in combination with an aluminum MCS for electrodynamic levitation purposes [10]–[13]. However, an analysis of a non-coaxial eddy-current coupling for a steel MCS in combination with the introduction of a computationally highly efficient simulation method has not been presented in literature so far.

In this paper, a semi-analytical method (SAM), which allows simulating system's characteristics and performance, is derived in Sec. II at first.

Subsequently, measurements on two prototypes, built such that they suit the desired application, are presented and compared to the results of the SAM as well as to the result of a time-transient finite element method (FEM) simulation in Sec. III. Moreover, insight into the significant performance improvement of the SAM, compared to a time-transient FEM is given. Additionally, a power density vs. efficiency (ρ-η) Pareto optimization for a design space with relaxed boundaries considering geometric properties of the PM wheel is performed in Sec. IV. Hence, recommendations on the design of an eddy-current coupling for different applications can be formulated.

II. MODELING

A common approach for calculating the excited eddy currents is the utilization of (commercial) FEM simulation (software). Analyzing the power transfer in the considered non-coaxial eddy-current coupling requires a transient, 3-D FEM simulation. A fine mesh is mandatory on the surface of the steel wheel, i.e. MCS, since the induced eddy currents are flowing in a skin depth in the mm-range (as confirmed later). As a result, simulating the eddy-current coupling under different operating parameters (OPs) is challenging. Therefore, in the following, a computationally efficient method is presented for calculating the magnetic field, induced eddy-current distribution and the resulting characteristics of the coupling in terms of transferred power and efficiency.

Based on initial models formulated for non-magnetic conductor materials [10]–[13], the solution for the flux density distribution is a superposition of the flux density distribution of the PM wheel in free space (source field) and a reflected field due to induced eddy currents. The modeling domain can be separated into three regions (cf. Fig. 2):

- a conductive region (moving conductive body/surface: MCS),
- a top region (air), where the source field is mapped on the boundary and
- a bottom region below the conductive region.

In the conductive region, the following equation for the magnetic flux density $\vec{B}$ must hold

$$\nabla \times \vec{B} = \mu_2 \sigma(\vec{E} + \vec{v} \times \vec{B}), \tag{1}$$

where $\mu_2 = \mu_0 \cdot \mu_{2,\mathrm{r}}$, σ and $\vec{v}$ are the conductive material's permeability, conductivity and speed, and $\vec{E}$ is the electric field strength.

In the non-conductive regions (top and bottom)

$$\nabla \times \vec{B} = 0 \tag{2}$$

must hold.

Clearly, Gauss' law for magnetism,

$$\nabla \cdot \vec{B} = 0, \tag{3}$$

must hold in all regions.

Moreover, for the non-conductive regions, a magnetic scalar potential ϕ can be defined, which simplifies the calculation of the flux density distribution,

$$\vec{B} = -\mu_2 \operatorname{grad}(\phi). \tag{4}$$

A convenient approach is to assume that the system is in steady state (implies constant/slowly changing rotational speed of the magnet wheel) and altering with an electrical frequency

$$\omega_\mathrm{e} = p \cdot \omega_1, \tag{5}$$

where p is the number of pole pairs and ω_1 the rotational frequency of the PM wheel.

Further, it allows introducing the flux density distribution as a phasor

$$\vec{B}(x, y, z, t) = Re\left\{\vec{B}(x, y, z) \cdot \mathrm{e}^{\mathrm{j}\,\omega_\mathrm{e}\, t}\right\}. \tag{6}$$

Generally, a set of partial differential equations for the three-dimensional flux density vector field must be solved for obtaining the solution of the problem in terms of flux density and eddy-current distribution. However, solving the problem in the Fourier domain, where the Fourier transforms of the flux density $B(x, y, z)$ and of the magnetic scalar potential $\phi(x, y, z)$ are introduced as

$$\begin{aligned}\vec{\mathcal{B}}(\xi, y, \zeta) &= \iint_{\mathbb{R}_2} \vec{B}(x, y, z) \cdot \mathrm{e}^{\mathrm{j}\xi y} \cdot \mathrm{e}^{\mathrm{j}\zeta z} dx\, dz, \\ \varphi(\xi, y, \zeta) &= \iint_{\mathbb{R}_2} \phi(x, y, z) \cdot \mathrm{e}^{\mathrm{j}\xi y} \cdot \mathrm{e}^{\mathrm{j}\zeta z} dx\, dz,\end{aligned} \tag{7}$$

allows replacing the set of partial differential equations by a set of linear equations.

The Fourier transformed field is solved and the solution transformed back to $B(x, y, z)$ numerically, with a fast Fourier transform.

As described, the flux density distribution of the PM wheel in free space is required as source field for the SAM calculation. In previous works [10], [12], [13], the source field is calculated analytically and then employed for finding the eddy-current distribution in the MCS. A significant limitation of this approach is that finding the source field solution can be cumbersome and requires an analytic derivation of the exact geometry of interest. This work follows a different paradigm and directly imports the source field from a stationary FEM simulation, which is computationally efficient, as no transient effects (e.g. induced eddy currents) have to be simulated. Therefore, the field is evaluated in the simulation software on planes around the PM wheel as illustrated in Fig. 3. Further, the Fourier transformed source field $\vec{\mathcal{B}}_\mathrm{src}$ (which was obtained by FEM) is applied on the boundary of the top region (cf. Fig. 2). Appendix A details the SAM and its analytic solution further.

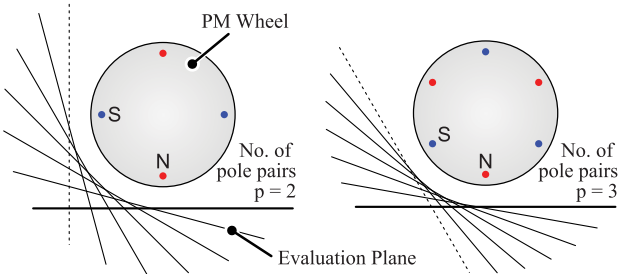

FIGURE 3. Location of field evaluation planes for pole pair numbers $p = 2$ and $p = 3$.

TABLE 1. Parameter for measurements.

Parameter	Var.	Meas. Series A	B	C
PM wheel rad.	r_1	25 mm		
PM wheel inner rad.	$r_{1,\mathrm{i}}$	15 mm		
PM wheel axial length	h	10 mm		
Number of pole pairs	p	2	3	
PM permeability	μ_mag	μ_0		
PM remanence	B_r	1.2 T		
PM conductivity	κ_mag	0 MS/m		
PM wheel core mat.		Steel		
Core mat. con'tivity	$\kappa_{1,\mathrm{i}}$	0		
Core mat. perm'bility	$\mu_{1,\mathrm{i}}$	500 μ_0		
Sec. radius	r_1	225 mm		
Sec. ax. length	$l_{\mathrm{y},2}$	60 mm		
MCS material		Ac-112		C45E
MCS conductivity	κ_2	26 MS/m		5 MS/m
MCS permeability	μ_2	μ_0		350 μ_0
Air gap	g	5 mm		3 mm
MCS speed	v_2	22.2 m/s		

In summary, the SAM approach allows rapidly simulating many different designs with arbitrary shapes and arbitrary magnetization as the versatility of FEM is combined with the superior computational performance of an analytic model. The computational merit of the SAM approach in comparison to a transient 3-D FEM simulation of a selected design is quantified in Sec. III-C.

III. PROTOTYPES AND MEASUREMENT/SAM RESULTS

The desired application on a freight wagon only allows a confined space for a PM wheel with a radius of $r_1 = 25$ mm and an axial length of $h = 10$ mm. Therefore, two prototypes (cf. Fig. 4b) were built and tested on a test setup depicted in Fig. 4a, which also allows validating the SAM by experiments. A wheel with a radius of $r_2 = 225$ mm is used as MCS, i.e. for the emulating the train wheel. The test setup allows adjusting MCS speed and air gap. In order to characterize the power transfer characteristic of the eddy-current coupling, the PM wheel is loaded with a generator as depicted in Fig. 4. Torque sensors with integrated speed resolvers are utilized to measure the mechanical power on input (between induction machine and MCS wheel) and output (between PM wheel and generator).

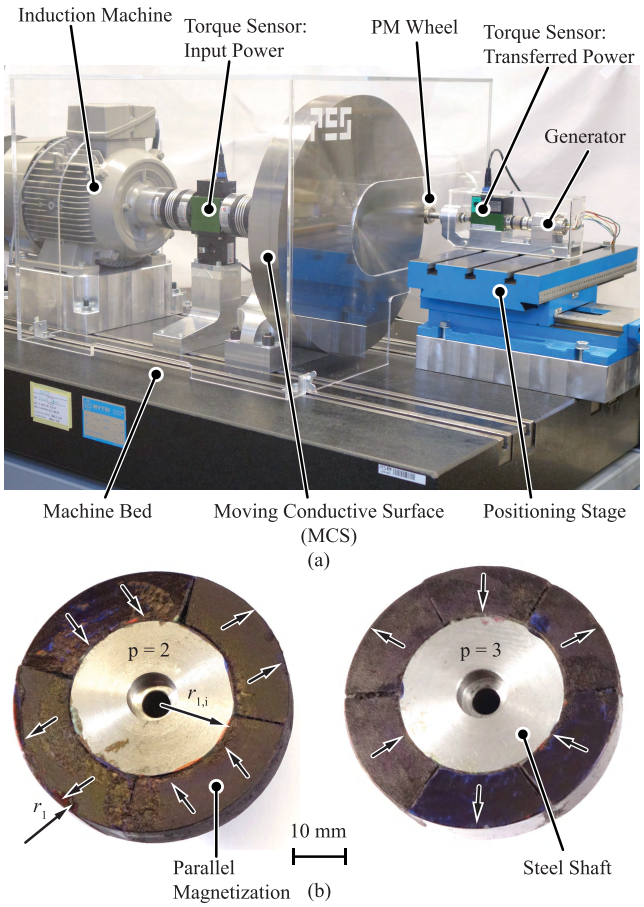

FIGURE 4. **(a) Test setup for verifying the SAM simulation model. As in the railway application, the MCS is not moving linearly but is a rotating wheel with significantly larger (≈ factor 10) radius $r_2 = 225$ mm than the PM wheel. A variable speed drive, formed by a commercially available induction machine and an inverter, drives the test setup. The PM wheel is then mounted on a fixture close to the radial surface of the MCS. The air gap can be adjusted with the shown positioning stage. (b) Built PM wheel prototypes according to Table 1 with pole pair numbers $p = 2$, 3. Both wheels show a PM wheel radius $r_1 = 25$ mm.**

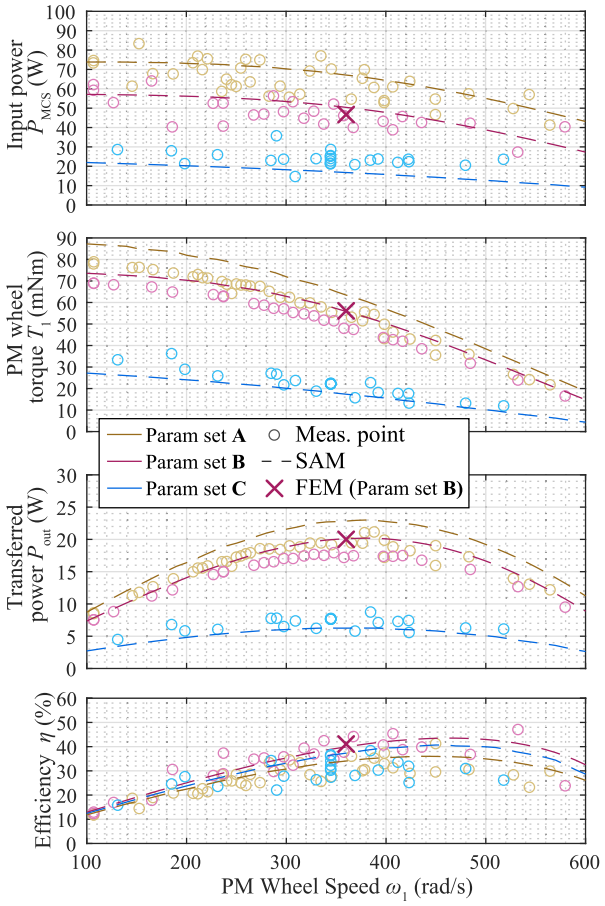

FIGURE 5. **Measurement series according to parameter sets A, B and C of Table 1. Parameter sets A and B are with an aluminum MCS, while C is with a steel MCS. Measurement noise is apparent on measurements of the drive side, as the measured input power is comparably low for the utilized drive system (induction machine, bearing arrangement). Good agreement between measurements, SAM and FEM simulations can be observed.**

Table 1 summarizes key parameters of the hardware prototypes, the test setup and the OPs for the measurement. The MCS speed was set to $v_2 = 22.2\,\text{m/s} = 80\,\text{km/h}$, which is a typical travel speed of a freight train.

In order to emulate the magnetic behavior of a wagon's wheel, the MCS is made of C45E steel (Mat. No. 1.1191, cf. [15]), which has a similar metallurgic composition as wagon wheels in Europe and Japan. Moreover, additional measurements were conducted with an aluminum wheel (Ac-112, Mat. No. 6082, cf. [16]), in order to illustrate the performance difference between different MCS materials.

A. MEASUREMENT RESULTS

Measurements of input and output power were taken while gradually loading the coupling. They are shown in Fig. 5. Friction torques due to the bearings on the drive shaft and on the mounting fixture for testing the PM wheel were compensated in the shown measurement results. Torques on the input and output increase with reducing the PM wheel speed ω_1 as the difference in surface speed between PM wheel and MCS increases. The achievable mechanical output power is significantly higher with an aluminum MCS than with the steel MCS due to the increased conductivity of the material. The prototype couplings' electromechanical efficiency,

$$\eta = \frac{P_{\text{out}}}{P_{\text{MCS}}}, \tag{8}$$

is in the range of 35 . . . 45% (in reasonable operating points) for all measurement series.

B. VERIFICATION OF SAM SIMULATION

In order to verify the derived SAM model, simulations were conducted for measurements according to Table 1 and results are depicted in Fig. 5 together with measurements. A good agreement could be found for both, aluminum and steel MCS with the set of used material parameters. The conductivity of steel C45E was measured on a rod-shaped specimen,

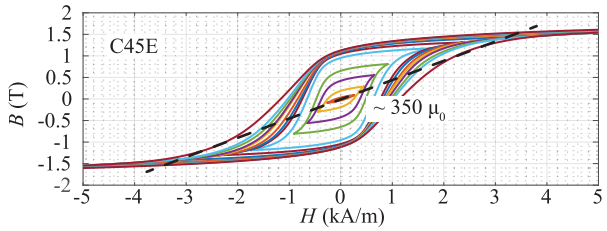

FIGURE 6. Measured hysteresis curves of steel C45E for 1 Hz AC magnetization [14]. The used linearized permeability value of 350 μ_0 of the simulation models is shown with a dashed line.

while a data sheet value was used for aluminum Ac-112. The SAM assumes a linear MCS permeability and therefore, it is a tuning parameter for the simulation, which has to be calibrated with measurements. Measured hysteresis curves of C45E are shown in Fig. 6. Measurements were conducted at 1 Hz on a C45E ring specimen. A relatively low permeability of $\mu_2 = 350\,\mu_0$ is resulting for the steel MCS in interaction with the PM wheel as only a small cross-section in the MCS is conducting flux during the system's operation. Simulations of the flux density in the MCS in Fig. 7 show that the flux is concentrated close to the surface of the MCS. Starting from a simulation of flux density distribution for the standstill of the system in Fig. 7a, the flux in the MCS is concentrated with increasing speed. Fig. 7b shows results for a reduced operating speed with $v_2 = 5\,\text{m/s}$. The final picture of a flux density distribution for the nominal operating point is given in Fig. 7c, where the skin effect is most pronounced and the maximum flux density reaches values well-above the PM remanence flux density B_r, i.e. 1.2 T.

C. COMPUTATIONAL MERIT

After validating the SAM simulation with measurements, the computational merit of the SAM shall be briefly studied. For one operation point, with $\omega_2 = 360\,\text{rad/s}$ of parameter set **B**, in addition to the SAM simulation (results depicted in Fig. 5), a 3-D, transient simulation with a commercially available FEM software was set up and conducted. The results are also given in Fig. 5 and one can see that measurement, SAM and FEM simulation agree. Both simulations, SAM and 3-D FEM, were conducted on a machine with two Quad-Core Intel Xeon E5620 CPUs and 96GB of installed RAM. Remarkable in the comparison between conducted FEM and SAM simulation is the difference in simulation time as given in Fig. 8. For the analyzed case, the SAM shows a significantly lower (factor $\approx$ 500 faster) computational burden.

D. INFLUENCE OF AIR GAP WIDTH AND MCS SPEED

Fig. 9 illustrates the couplings' operation outside the specified set of OPs in terms of MCS speed and air gap width. Points of maximum transferred power are plotted. In this simulation, it was obtained by a grid search over PM wheel speed ω_1, while in a system implementation, it can be performed with a maximum power point tracking algorithm (MPPT) [17]–[20]. Clearly, a larger air gap leads to a decay in power

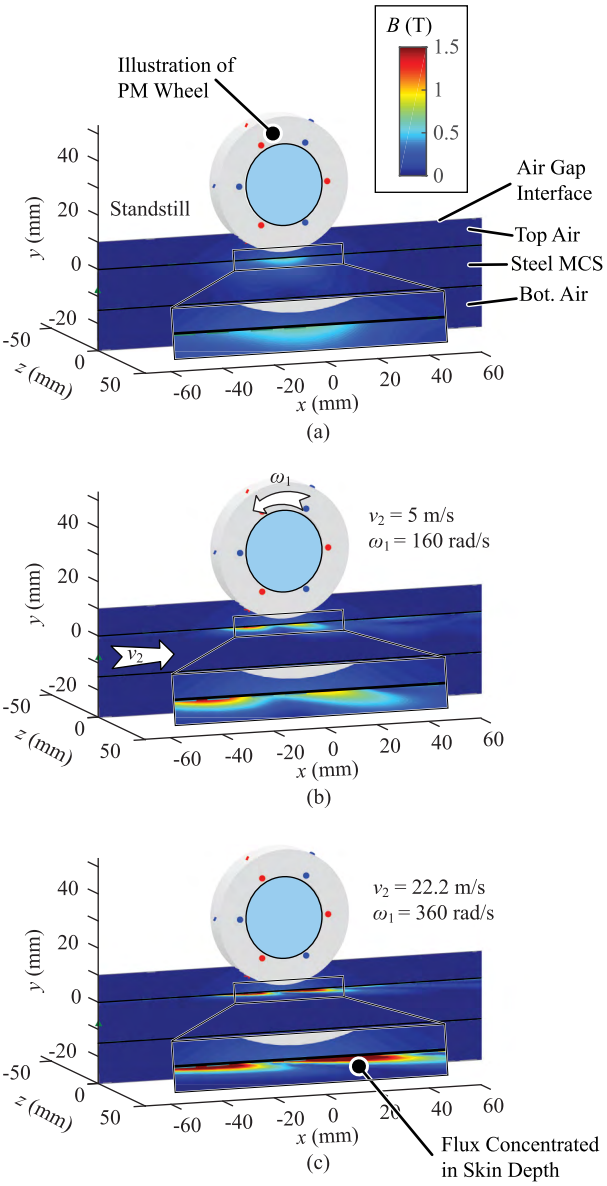

FIGURE 7. Illustration of flux density in the simulation region; simulations of the PM wheel, according to Table 1 C. (a) flux density distribution of the system at standstill. (b) flux density distribution at a reduced operating speed of MCS and PM wheel. It can be observed that the flux density in the MCS increases (compared to the standstill) and that the flux density concentrates close to the MCS surface. (c) simulation results for the nominal operating point of the system.

transfer capability (cf. Fig. 9a). It can be observed that an increase of 2 mm in air gap width approximately reduces the transferred power by a factor of 2. Moreover, in the analyzed cases, the power transfer capability with an aluminum wheel (parameter set **B**) was found to be approx. 5 times higher than the power transfer capability with a steel wheel (parameter set **C**).

The increase in power transfer capability with increasing speed is analyzed and shown in Fig. 9b. The increase in power is approximately linear with MCS speed.

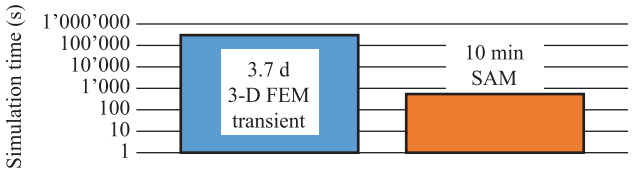

FIGURE 8. Illustration of computational merit of the introduced SAM. For one simulation point, a simulation with the SAM and a simulation with a full transient 3-D eddy-current simulation was conducted on a machine with two Quad-Core Intel Xeon E5620 CPUs and 96GB of installed RAM. The duration of simulation is shown in the bar graph. For the analyzed case, the SAM shows a significant improvement (factor ≈ 500 faster) in computational burden.

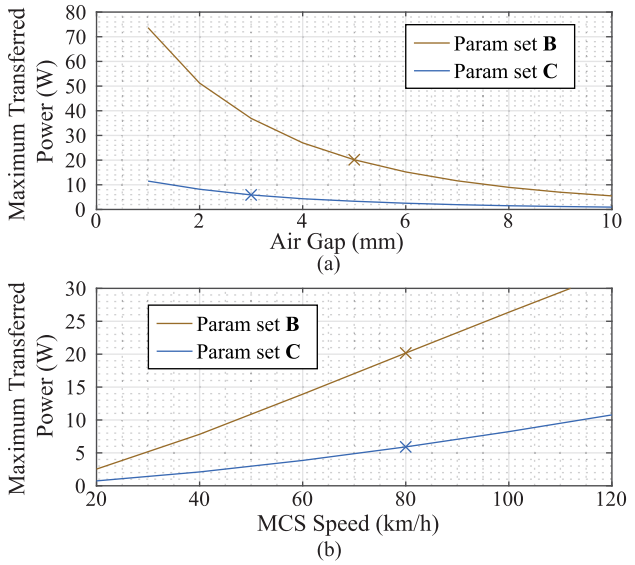

FIGURE 9. Influence of air gap and with MCS speed on the maximum transferable power. Parameters for the simulation are in accordance with Table 1. Parameter set B is for an aluminum MCS and parameter set C is for a steel MCS. Markers 'x' denote the nominal operating point in air gap and speed of parameter sets B and C in Fig. 5, respectively.

IV. DESIGN FOR RELAXED PARAMETER CONSTRAINTS

In order to broaden the study, a $\rho\eta$-Pareto optimization of the system is conducted for a relaxed design space (no constraints on the size of the PM wheel) and for higher output power of $P_{\text{target}} = 10\,\text{W}$. Sweep parameters for the optimization are summarized in Table 2. More than 1000 designs were simulated and evaluated. Simulations were conducted with the introduced SAM and the coupling's performance is analyzed in terms of power density ρ and efficiency η. The results are compiled in Fig. 10. Designs fulfilling $P_{\text{target}} < P_{\text{out}} < P_{\text{target}} \cdot 110\%$ are shown. The PM wheel's power density was calculated as

$$\rho = \frac{P_{\text{target}}}{r_1^2\,\pi\,h}, \tag{9}$$

where r_1 is the PM wheel outer radius and h its axial length.

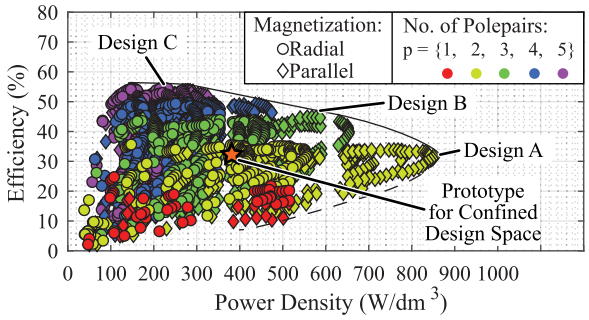

FIGURE 10. Pareto analysis in a power density ρ - efficiency η plane for $P = 10\,\text{W}$ output power and interaction of the PM wheel with a C45E steel MCS with $v = 80\,\text{km/h}$ surface velocity and an air gap width of $g = 3\,\text{mm}$. Designs of the PM wheels were swept according to the parameter set Table 2. Two selected designs (A,B) are indicated in the diagram and relaxed parameters are given in Table 3. Moreover, the characteristic of the built prototype for the confined design space in the target application (cf. Table 1; Measurement Series C) is also depicted in the ρ-η plane.

TABLE 2. Parameter set for the pareto analysis.

Parameter	Variable	Value
PM wheel rad.	r_1	$10 \ldots 40\,\text{mm}$
Iron core radius	$r_{1,\text{i}}$	$(0.2 \ldots 0.9)\,r_1$
MCS surf. veloc.	v_2	$22.2\,\text{m/s}$
Air gap	g	$3\,\text{mm}$
Number of pole pairs	p	$1, 2 \ldots 5$
Axial length	h	$5\,\text{mm} \ldots 50\,\text{mm}$

TABLE 3. Key parameters of selected systems A, B and C.

Parameter	Var.	Design A	Design B	Design C
PM wheel rad.	r_1	14 mm	17 mm	17 mm
Inner rad.	$r_{1,\text{i}}$	4 mm	5 mm	8.5 mm
PM wheel depth	h	21 mm	20 mm	51 mm
Pole pairs	p	2	3	5
Efficiency	η	32 %	45 %	54 %
Power Density	ρ (W/dm^3)	850	590	220

Both, PM wheels with radial (magnetization direction truly in a radial direction for each point in the magnet segment) and parallel (magnetization parallel for a magnet segment; cf. Fig. 4b) magnetization were simulated. Three optimized designs (Design A, B, C) are picked from the optimization and their parameters are given in Table 3. Design A shows high power density, while design C shows higher efficiency. Design B is a compromise between power density and efficiency.

The optimization shows that parallel magnetization and a pole pair number of 2 shows high power density, while higher efficiency is achieved with radial magnetization and a higher number of pole pairs. The efficiency (cf. (8)) was found to be bound by $\approx 60\,\%$.

V. CONCLUSION

A non-coaxial eddy-current coupling, comprising a permanent magnet (PM) wheel and a moving conductive

body/surface (MCS) and a computationally efficient semi-analytical (simulation) method (SAM) were presented in this work. The target application for employing the coupling is auxiliary power generation on a freight train wagon, where the MCS would be a moving surface of the wagon's wheel. The PM wheel would be installed next to it, forming the eddy-current coupling.

The SAM is introduced in order to calculate the transferred power and losses of the coupling. It allows solving the 3-D field equations of the problem in the Fourier domain, which leads to a computationally efficient set of linear equations. Further, the derived equations can be solved numerically in an efficient way. A case study shows that the SAM is about 500 times faster than a transient 3-D eddy-current simulation, conducted with a commercially available FEM software.

Two prototypes, suitable for the desired application were built and tested and the conducted measurement series verify the introduced SAM. Moreover, a linear dependency of transferred power on the MCS speed was identified.

Overall, the SAM approach combines the versatility of FEM with the superior computational performance of an analytic model and hence, a design optimization for relaxed parameter constraints is conducted. The study reveals that power densities of up to 800 $\mathrm{W/dm^3}$ (13 $\mathrm{W/in^3}$), considering the volume of the PM wheel only, can be achieved for extracting power over an air gap width of $g = 3\,\mathrm{mm}$ from an MCS made of C45E steel and moving with a surface velocity of $v = 80\,\mathrm{km/h} = 22.2\,\mathrm{m/s}$. Moreover, the investigation shows that the efficiency of such system is limited to $\approx 60\,\%$ for typical scenarios. It can be concluded that PM wheels with parallel magnetization and pole pair numbers of $p = 2$ and 3 show the best performance in an efficiency-power-density trade-off.

In summary, this paper presents an extensive analysis of a non-coaxial eddy-current coupling for its utilization in an auxiliary power supply system and presents a computationally highly efficient method for solving the arising 3-D and transient field problem.

ACKNOWLEDGMENT

The authors would like to express their sincere appreciation to Nabtesco Corporation, Japan, Kyoto, Japan, for the financial and technical support of research on energy harvesting technologies at the Power Electronic Systems Laboratory, ETH Zurich, which provided the basis for achieving the results presented in this paper. In particular, inspiring technical discussions with K. Nakamura, Y. Tsukada and Y. Ono are acknowledged.

APPENDIX
DERIVATION OF SAM

In addition to the briefly summarized modeling approach in Sec. II, the equations required for the SAM model are derived in the following.

With the Maxwell-Faraday equation

$$\frac{\partial}{\partial t}\vec{B} = -\nabla \times \vec{E},$$

(2) can be reformulated as

$$\nabla \times \nabla \times \vec{B} = \mu_2\sigma(-\frac{\partial}{\partial t}\vec{B} + \nabla \times \vec{v} \times \vec{B}). \tag{10}$$

With expanding the curls, (10) can be rewritten as

$$(\partial_{xx} + \partial_{yy} + \partial_{zz})\vec{B} = \mu_2\sigma(\mathrm{j}\omega_e\vec{B} + \vec{v} \cdot \mathrm{div}(\vec{B})). \tag{11}$$

For obtaining the solution of the field problem, a two-dimensional Fourier transform of the magnetic field $B(x, y, z)$ and the magnetic scalar potential $\phi(x, y, z)$ was introduced in (7).

Therefore, (11) can be rewritten as

$$\frac{\partial^2}{\partial y^2}\vec{\mathcal{B}} - \underbrace{(\xi^2 + \zeta^2 + \mathrm{j}\mu_2\sigma(\omega_e + \xi v_x + \zeta v_z))}_{\gamma^2}\vec{\mathcal{B}} = 0, \tag{12}$$

with $j \in x, y, z$ and $v_y = 0$.

With the ansatz $\mathrm{e}^{\beta y}$ for the y-dependency (12) becomes a polynomial in β:

$$\frac{\partial^2\vec{\mathcal{B}}}{\partial y^2} - \gamma^2\vec{\mathcal{B}} = 0 \Longrightarrow \beta^2 - \gamma^2 = 0 \tag{13}$$

Its roots are $\beta_{1,2} = \pm\gamma$; for convenience, we define $\beta = \gamma$ and obtain the general Fourier-domain solution for the fields in the conductor,

$$\vec{\mathcal{B}}_{\mathrm{cond}}(\xi, y, \zeta) = \vec{C}_{\mathrm{cond}}(\xi, \zeta) \cdot \mathrm{e}^{\beta \cdot y} + \vec{D}_{\mathrm{cond}}(\xi, \zeta) \cdot \mathrm{e}^{-\beta \cdot y}, \tag{14}$$

with

$$\beta = \sqrt{\xi^2 + \zeta^2 + \mathrm{i}\mu_2\sigma\,(\omega_e + \xi v_x + \zeta v_z)} \in \mathbb{C}. \tag{15}$$

It shall be noted that the vectorial constants $\vec{C}_{\mathrm{cond}}(\xi, \zeta)$ and $\vec{D}_{\mathrm{cond}}(\xi, \zeta)$ are still unknown.

Gauss's Law (3) must also hold for the flux density distribution with the provided ansatz and can be reformulated as

$$\begin{aligned}\begin{bmatrix}\mathrm{j}\xi & \beta & \mathrm{j}\zeta\end{bmatrix}\vec{C}_{\mathrm{cond}} &= 0,\\ \begin{bmatrix}\mathrm{j}\xi & -\beta & \mathrm{j}\zeta\end{bmatrix}\vec{D}_{\mathrm{cond}} &= 0.\end{aligned} \tag{16}$$

Invoking the definition of the magnetic scalar potential (4), Gauss's Law for the non-conductive region results in

$$(\partial_{xx} + \partial_{yy} + \partial_{zz})\phi = 0 \implies (\alpha^2 - \xi^2 - \zeta^2)\varphi = 0. \tag{17}$$

Similar to the solution described in (14) for the conductive region, solutions for the air region above and under the conductive region, $\vec{\mathcal{B}}_{\mathrm{air}}$ and $\vec{\mathcal{B}}_{\mathrm{bot}}$ (cf. "top region" and "bottom region" in Fig. 2), can be described as

$$\vec{\mathcal{B}}_{\mathrm{air}} = \vec{\mathcal{B}}_{\mathrm{src}} + \begin{pmatrix}\mathrm{j}\xi\\ -\alpha\\ \mathrm{j}\zeta\end{pmatrix} D_{\mathrm{air}}(\xi, \zeta)\,\mathrm{e}^{-\alpha y}, \tag{18}$$

$$\vec{\mathcal{B}}_{\mathrm{bot}} = \begin{pmatrix}\mathrm{j}\xi\\ \alpha\\ \mathrm{j}\zeta\end{pmatrix} C_{\mathrm{air}}(\xi, \zeta)\,\mathrm{e}^{\alpha y}, \tag{19}$$

both with

$$\alpha = \sqrt{\xi^2 + \zeta^2} \in \mathbb{C}. \tag{20}$$

Constants D_{air} and C_{air} are scalar. The source term, which describes the excitation due to the PM wheel is taken into account with $\vec{\mathcal{B}}_{\text{src}}$ in (18).

The continuity of the magnetic field on top of the conductive region ($y = 0$) and on the lower edge of the conductive region ($y = -d$) are accounted with

$$\vec{\mathcal{B}}_{\text{cond}}(y=0) = \begin{pmatrix} \mu_{2,\text{r}} \\ 1 \\ \mu_{2,\text{r}} \end{pmatrix} \vec{\mathcal{B}}_{\text{air}}(y=0), \tag{21}$$

$$\vec{\mathcal{B}}_{\text{cond}}(y=-d) = \begin{pmatrix} \mu_{2,\text{r}} \\ 1 \\ \mu_{2,\text{r}} \end{pmatrix} \vec{\mathcal{B}}_{\text{bot}}(y=-d). \tag{22}$$

With the provided approach, only constants $\vec{C}_{\text{cond}}, \vec{D}_{\text{cond}}, D_{\text{air}}$ and C_{air} have to be found, such that the field problem can be solved. In summary, 8 scalar unknown variables have to be found, while a set of 8 scalar equations is present with (16), (21) and (22). Numerically, this results in solving the matrix equation

$$\begin{bmatrix} \mu_{2,\text{r}}\text{i}\xi & -1 & -1 & 0 & 0 & 0 & 0 & 0 \\ \alpha & 0 & 0 & 1 & 1 & 0 & 0 & 0 \\ \mu_{2,\text{r}}\text{i}\zeta & 0 & 0 & 0 & 0 & -1 & -1 & 0 \\ 0 & \text{e}^{-\beta d} & \text{e}^{\beta d} & 0 & 0 & 0 & 0 & -\mu_{2,\text{r}}\text{i}\xi\ \text{e}^{-\alpha d} \\ 0 & 0 & 0 & \text{e}^{-\beta d} & \text{e}^{\beta d} & 0 & 0 & -\alpha\ \text{e}^{-\alpha d} \\ 0 & 0 & 0 & 0 & 0 & \text{e}^{-\beta d} & \text{e}^{\beta d} & -\mu_{2,\text{r}}\text{i}\zeta\ \text{e}^{-\alpha d} \\ 0 & \text{i}\xi & 0 & \beta & 0 & \text{i}\zeta & 0 & 0 \\ 0 & 0 & \text{i}\xi & 0 & -\beta & 0 & \text{i}\zeta & 0 \end{bmatrix} \cdot \begin{bmatrix} D_{\text{air,ref}} \\ C_{\text{cond},x} \\ D_{\text{cond},x} \\ C_{\text{cond},y} \\ D_{\text{cond},y} \\ C_{\text{cond},z} \\ D_{\text{cond},z} \\ C_{\text{air}} \end{bmatrix} = \begin{bmatrix} -\mu_{2,\text{r}}\mathcal{B}_{\text{src},x} \\ \mathcal{B}_{\text{src},y} \\ -\mu_{2,\text{r}}\mathcal{B}_{\text{src},z} \\ 0 \\ 0 \\ 0 \\ 0 \\ 0 \end{bmatrix}. \tag{23}$$

With solving unknown constants (C_i, D_i) in (23), the flux density distribution can be expressed in the Fourier-domain and then transformed back in the space domain $\vec{B}(x, y, z, t)$ with FFT. With evaluating the Maxwell stress tensor on top of the MCS ($y = 0$), a surface force density of

$$\vec{f}_{\text{Maxwell}} = \begin{pmatrix} \tau_{\text{x}} \\ \sigma_{\text{y}} \\ \tau_{\text{z}} \end{pmatrix} = \frac{1}{\mu_0} \begin{pmatrix} B_{\text{x}}\, B_{\text{y}} \\ B_{\text{y}}^2 - B_{\text{x}}^2 - B_{\text{z}}^2 \\ B_{\text{y}}\, B_{\text{z}} \end{pmatrix} \tag{24}$$

results.

The power generating/consuming force on the MCS is found by integrating τ_{x} over the MCS surface

$$F_x = \int_{A_{\text{MCS}}} \tau_{\text{x}}\, \text{d}A. \tag{25}$$

Consequently, the input power is

$$P_{\text{MCS}} = F_x\, v_2. \tag{26}$$

The torque on the PM wheel can be calculated in a similar approach [2] as

$$T_1 = \vec{\text{e}}_z \cdot \int_{A_{\text{MCS}}} (\vec{r} - \vec{r}_{\text{ax}}) \times \vec{f}_{\text{Maxwell}}\, \text{d}A, \tag{27}$$

where $\vec{\text{e}}_z$ is the unit vector in z-direction, $\vec{r}$ the coordinate of the point of evaluation and $\vec{r}_{\text{ax}}$ the coordinate of the PM wheel axis. Finally, the transferred power is

$$P_{\text{out}} = T_1 \cdot \omega_1. \tag{28}$$

REFERENCES

[1] M. R. Elhebeary, M. A. A. Ibrahim, M. M. Aboudina, and A. N. Mohieldin, "Dual-source self-start high-efficiency microscale smart energy harvesting system for IoT," *IEEE Trans. Ind. Electron.*, vol. 65, no. 1, pp. 342–351, Jun. 2018.

[2] M. Flankl, A. Tüysüz, I. Subotic, and J. W. Kolar, "Novel contactless axial-flux permanent-magnet electromechanical energy harvester," in *Proc. Conf. Expo. Appl. Power Electron. (APEC)*, Mar. 2016, pp. 623–630.

[3] T. Searle, T. Yildirim, M. H. Ghayesh, W. Li, and G. Alici, "Design, fabrication, and test of a coupled parametric–transverse nonlinearly broadband energy harvester," *IEEE Trans. Energy Convers.*, vol. 33, no. 2, pp. 457–464, Jun. 2018.

[4] J. Moon and S. B. Leeb, "Enhancement on energy extraction from magnetic energy harvesters," in *Proc. IEEE Energy Conv. Conf. Expo. (ECCE-USA)*, Sep. 2015, pp. 427–433.

[5] D. Strothmann, "Device for contactless current generation, in particular bicycle dynamo, vehicle lighting system and bicycle," DE Patent 2013/004 320 A1, Jan. 10, 2013.

[6] T. Lubin and A. Rezzoug, "Steady-state and transient performance of axial-field eddy-current coupling," *IEEE Trans. Ind. Electron.*, vol. 62, no. 4, pp. 2287–2296, Apr. 2015.

[7] J. Wang and J. Zhu, "A simple method for performance prediction of permanent magnet eddy current couplings using a new magnetic equivalent circuit model," *IEEE Trans. Ind. Electron.*, vol. 65, no. 3, pp. 2487–2495, Mar. 2018.

[8] Z. Mouton and M. J. Kamper, "Modeling and optimal design of an eddy current coupling for slip-synchronous permanent magnet wind generators," *IEEE Trans. Ind. Electron.*, vol. 61, no. 7, pp. 3367–3376, Jul. 2014.

[9] M. Flankl, A. Tüysüz, and J. W. Kolar, "Analysis of a watt-range contactless electromechanical energy harvester facing a moving conductive surface," in *Proc. IEEE Energy Conv. Expo. (ECCE-USA)*, Sep. 2015, pp. 414–420.

[10] N. Paudel, "Dynamic suspension modeling of an eddy-current device: An application to maglev," Ph.D. dissertation, Univ. North Carolina, Charlotte, Charlotte, NC, USA, 2012.

[11] S. Paul, W. Bomela, N. Paudel, and J. Z. Bird, "3-D eddy current torque modeling," *IEEE Trans. Magn.*, vol. 50, no. 2, pp. 905–908, Feb. 2014.

[12] N. Paudel and J. Z. Bird, "General 2-D steady-state force and power equations for a traveling time-varying magnetic source above a conductive plate," *IEEE Trans. Magn.*, vol. 48, no. 1, pp. 95–100, Jan. 2012.

[13] N. Paudel, J. Bird, S. Paul, and D. Bobba, "A transient 2D model of an electrodynamic wheel moving above a conductive guideway," in *Proc. IEEE Int. Electr. Machines Drives Conf. (IEMDC)*, May 2011, pp. 545–550.

[14] M. Flankl, A. Tüysüz, and J. W. Kolar, "Impact of iron dust on electromechanical systems: A case study," in *Proc. IEEE Southern Power Electron. Conf. (SPEC)*, Dec. 2016, pp. 1–8.

[15] *Steels for Quenching and Tempering*, Standard EN 10 083-1, European Committee Standardization, 2006.

[16] *Aluminium and Aluminium Alloys. Chemical Composition and Form of Wrought Products*. Chemical Composition Products, Standard EN 573-3, 2013.

[17] B. Bijukumar, R. A. G. Kaushik, I. G. Saravana, and C. Nagamani, "A linear extrapolation based MPPT algorithm for thermoelectric generators under dynamically varying temperature conditions," *IEEE Trans. Energy Convers.*, to be published. [Online]. Available: https://ieeexplore.ieee.org/document/8351979/

[18] J. Hussain and M. K. Mishra, "Adaptive maximum power point tracking control algorithm for wind energy conversion systems," *IEEE Trans. Energy Convers.*, vol. 31, no. 2, pp. 697–705, Jun. 2016.
[19] F. Keyrouz, "Enhanced Bayesian based MPPT controller for PV systems," *IEEE Power Energy Technol. Syst. J.*, vol. 5, no. 1, pp. 11–17, Mar. 2018.
[20] N. D. Tuyen and G. Fujita, "PV-active power filter combination supplies power to nonlinear load and compensates utility current," *IEEE Power Energy Technol. Syst. J.*, vol. 2, no. 1, pp. 32–42, Mar. 2015.

MICHAEL FLANKL (S'12) received the B.Sc. degree in mechatronics from JKU Linz, Austria, in 2012, and the M.Sc. degree in robotics, systems & control from the Swiss Federal Institute of Technology (ETH) Zurich in 2014, where he is currently pursuing the Ph.D. degree with the Power Electronic Systems Laboratory. From 2010 to 2012, he was a freelancer at the Electrical Engineering/Electronics Department, Engineering Center Steyr GmbH (a branch of Magna Powertrain), St. Valentin, Austria. He is supervised by Prof. J. W. Kolar and involving in electrodynamic energy harvesting from moving conductive surfaces. His research interests and professional experience include special electric machines, drives, railway and automotive transportation systems, and optimization and control thereof.

ARDA TÜYSÜZ (S'10–M'13) received the B.Sc. degree in electrical engineering from Istanbul Technical University, Istanbul, Turkey, in 2006, the M.Sc. degree in electrical power engineering from RWTH Aachen University, Aachen, Germany, in 2009, and the Ph.D. degree in electrical drives from the Swiss Federal Institute of Technology (ETH) Zurich, Zürich, Switzerland, in 2015. After obtaining his Ph.D. degree, he was a Post-Doctoral Researcher with the Power Electronic Systems Laboratory, ETH Zurich, until 2017. His research interests during these period included novel electrical machine topologies, self-sensing control of high-speed electrical machines, electrical drives with very high signal-to-noise ratio, and wide-bandgap power devices for very efficient and compact electrical drive systems.

CHENG GONG received the B.Sc. and M.Sc. degrees in electrical engineering from Shanghai Jiao Tong University, Shanghai, China, in 2012 and 2014, respectively, and the M.Sc. degree in electrical and computer engineering from the Georgia Institute of Technology, Atlanta, GA, USA, in 2015, where he is currently pursuing the Ph.D. degree in electric machines and power electronics with Prof. Habetler. His research interests include ultra-high speed machines and electromagnetic simulations.

TIBOR STOLZ received the degree in electrical engineering from the Swiss Federal Institute of Technology (ETH) Zurich, Zürich, Switzerland, with a focus on power electronics, electric drives, and renewable energy. In his master's thesis, he developed analytical eddy-current models for various applications in mechatronics, including a graphical user interface for easy access to the simulations. Since 2017, he has been with the Power Electronic Systems Laboratory, ETH Zurich, extending this project as a Scientific Assistant.

JOHANN W. KOLAR (M'89–SM'04–F'10) received the Ph.D. degree *(summa cum laude)* in electrical engineering from the Vienna University of Technology, Austria. He is currently a Full Professor and the Head of the Power Electronic Systems Laboratory, Swiss Federal Institute of Technology (ETH) Zurich. He has proposed numerous novel PWM converter topologies and modulation and control concepts and has supervised over 60 Ph.D. students. He has published over 750 scientific papers in international journals and conference proceedings and three book chapters. He has filed more than 150 patents. He has presented over 20 educational seminars at leading international conferences. The focus of his current research is on ultra-compact and ultra-efficient SiC and GaN converter systems, wireless power transfer, solid-state transformers, power supplies on chip, and ultra-high speed and ultra-lightweight drives, bearingless motors, and energy harvesting. He has received the 25 IEEE Transactions and Conference Prize Paper Awards, the 2014 IEEE Power Electronics Society R. David Middlebrook Achievement Award, the 2016 IEEE William E. Newell Power Electronics Award, the 2016 IEEE PEMC Council Award, and two ETH Zurich Golden Owl Awards for excellence in teaching. He has initiated and/or is the founder of four ETH spin-off companies. He has served as the IEEE PELS Distinguished Lecturer from 2012 to 2016.